Bulletin of the Seismological Society of America, Vol. 99, No. 1, pp. 148–158, February 2009, doi: 10.1785/0120080055

Investigation of Fault Mechanisms during Geothermal Reservoir Stimulation Experiments in the Cooper Basin, Australia

by Stefan Baisch, Robert Vörös, Ralph Weidler, and Doone Wyborn

Abstract Subsequent to an initial reservoir stimulation in 2003, a second long-term fluid-injection experiment was conducted in the Cooper Basin, Australia, in 2005 to further enhance and enlarge the existent geothermal reservoir. Approximately $25,000\ m^3$ of water were injected into the granitic crust at 4250 m depth, thereby inducing about 16,000 seismic events, which were recorded by a local eight-station network. Event magnitudes calibrated by recordings of the permanent network of Geosciences Australia are in the range between $M_L -1.2$ and 2.9 with seismic moments between 10^9 and 10^{13} N m. Hypocenter locations could be determined for 8886 events. The spatial hypocenter distribution indicates that the seismicity occurred on the same subhorizontal layer structure identified for the initial reservoir stimulation, which is further extended in the course of restimulation.

Early seismicity is located near the outer rim of the previous zone of seismic activity and subsequently migrates both toward and away from the injection well. The immediate vicinity of the injection well remains seismically quiet during restimulation. These effects can be explained by a simple Kaiser effect model, where the induced seismicity is controlled by the *in situ* fluid pressure increase.

Compound fault-plane solutions based on *P*-phase polarities indicate a similar fault mechanism for nearly all events. The dominating fault mechanism is consistent with the regional stress field acting on a larger scale fracture zone with an orientation as outlined by the hypocenter distribution. A small number of events with reverse mechanisms might indicate the existence of conjugated fractures locally intersecting the main fracture zone. Cumulative slip determined by mapping the slip contribution of individual events onto the fracture zone indicates that most fracture patches in the reservoir slipped repeatedly, accumulating up to several centimeters of shear displacement.

Introduction

The Cooper Basin geothermal field is located in the northeast of South Australia near the Queensland border. Geothermal exploration started in the year of 2002, and to date three deep wells have been drilled into the granite to a depth level of 4200–4400 m. To enhance the hydraulic permeability between the injection well, Habanero 1, and the production well, Habanero 2, the injection well was hydraulically stimulated in 2003 thereby inducing about 28,000 detected microearthquakes. In a previous article (Baisch, Weidler, Vörös, Wyborn, and DeGraaf, 2006), we have analyzed hypocenter locations of about 11,000 of these events and found evidence that the induced seismicity aligns along a single, subhorizontal fracture zone. Logging data acquired before the stimulation (D. Wyborn, unpublished data, 2003) indicate that the fracture zone is of natural (tectonic) origin and already existed before reservoir activities started in the Cooper Basin. For this scenario, one could expect very similar source mechanisms for the induced seismicity. A detailed analysis of source mechanisms, however, could not be performed because instrument polarities were not known and might have changed in the course of channel reconfiguration during the experiment (for details, see Baisch, Weidler, Vörös, Wyborn, and DeGraaf, 2006).

In April 2005, a new data recording system was installed and has been continuously operated since then. Approximately 16,000 seismic events were recorded during restimulation activities of the Habanero 1 well in September 2005. Based on these events, we demonstrate that the source mechanisms are indeed extremely similar and consistent with the regional stress field acting on a larger scale fracture zone with an orientation as outlined by the hypocenter distribution. A small number of events with reverse mechanisms

might indicate the existence of conjugated fractures locally intersecting the main fracture zone. The spatiotemporal characteristics of the induced seismicity during restimulation provide important constraints on hydromechanical processes. We find evidence for stress relaxation (Kaiser effect) dominating the spatiotemporal evolution of seismicity during restimulation. Simple considerations of the hydraulic pressure distribution indicate that the same physical process could also explain the observed phenomenon of reverse hypocenter migration (i.e., toward the injection well). Mapping source area and slip associated with individual earthquakes onto the fracture zone indicates repeated slip on most patches of the stimulated fracture zone accumulating up to several centimeters of shear slip.

Seismic Monitoring System

In April 2005 the previous data recording system was replaced. Each seismic station was equipped with a three-channel 24 bit digitizer (type SMART24) recording continuously at a sampling rate of 500 Hz. Continuous waveform recordings are stored locally on a hard disk and are additionally transmitted by a wireless local area network (WLAN) to the central data acquisition office located at Habanero 1. At the time of writing, the data acquisition system has been operating without downtime, providing a complete record of the local seismicity since April 2005. Figure 1 shows the location of the seismic monitoring stations. The station geometry is essentially the same as reported previously except for the instruments at stations MW01, MW02, and MW03, which are deployed at a slightly shallower depth.

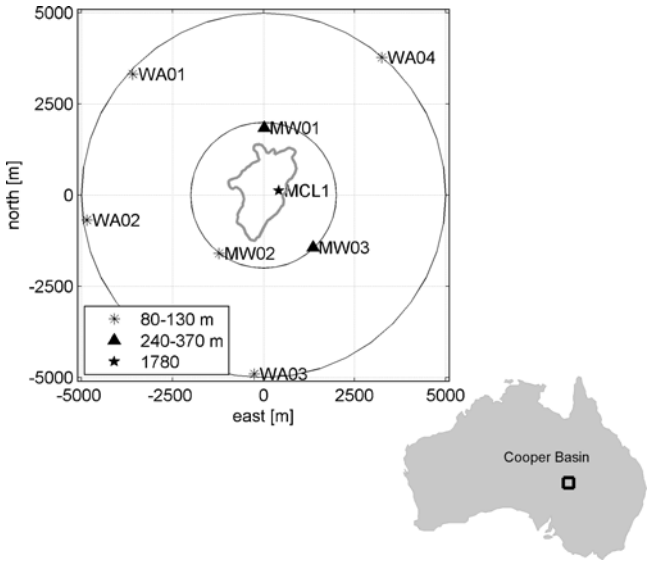

Figure 1. Location of the Cooper Basin (lower inset) and seismic station network in map view. Injection well (Habanero 1) is located at the origin of the local coordinate system (27°48′59″ S/140°45′35″ E). Legend annotates instrument depths. The region of 2003 seismic activity is indicated by a gray contour line.

Hydraulic Restimulation of Habanero 1

Starting in mid-September 2005 and continuing for 13 days, the Habanero 1 well was restimulated by injecting a total amount of $22,500$ m^3 of water into the 4421 m deep well. Maximum flow rates exceeded 31 L/sec and the wellhead pressure reached peak values close to 62 MPa (Fig. 2). This was the second hydraulic treatment of the Habanero 1 well (for details of the first treatment, we refer to Baisch, Weidler, Vörös, Wyborn, and DeGraaf [2006]) with the objective to extend the previously stimulated reservoir and to further enhance the hydraulic permeability. Although the entire 300 m long open hole section was hydraulically pressurized, flow velocity profiles along the wellbore indicated that the fluid entered the formation only in a zone around 4254 m depth where the well intersects a major fracture zone. Previous hydraulic testing of this fracture zone in 2003 revealed an extremely high artesian pressure of about 35 MPa above hydrostatic. The same overpressure was observed immediately before the injection (Fig. 2, middle panel).

During the 2005 injection period, a total number of approximately 16,000 seismic events were induced. Unlike the injection in 2003, seismic activity did not start immediately but was delayed by nearly 1 day (Fig. 2). Event detection rates were similar to those observed during the 2003 injection, with maximum rates exceeding 2000 events/day. It should be noted, however, that the signal detection threshold of the station network has changed due to the modification described in the previous section. In particular, replacing analogue signal transmission (landlines) by WLAN telemetry significantly improved the detection limit of the seismic network. Therefore, we assume that the actual seismicity rate was smaller than during the 2003 injection. This is consistent with the maximum event magnitudes determined at stations of the permanent network operated by the Australian government (Geosciences Australia). During the 2003 operations, 12 induced events were observed at these stations and assigned magnitudes between 2.5 and 3.7. For the current time period, only three events with magnitudes of 2.5, 2.9, and 3.0 were reported by Geosciences Australia.

We have used these three events to calibrate local magnitude M_L following the original definition as formulated by Gutenberg and Richter (1956):

$$M_L = \log A - \log A_{ref} + M_{ref}, \tag{1}$$

where A and A_{ref} denote maximum seismogram amplitudes and M_L and M_{ref} denote the associated magnitudes. Attenuation correction terms were not implemented because hypocentral distances are approximately the same for all events. The resulting magnitudes cover a range between M_L −1.2 and 2.9 (Fig. 3). We have also estimated the seismic moment for a data subset of approximately 6000 events with the highest data quality. By matching P-wave displacement spectra with an ω^2 model, we determined seismic moments and a frequency independent Q following the approach of

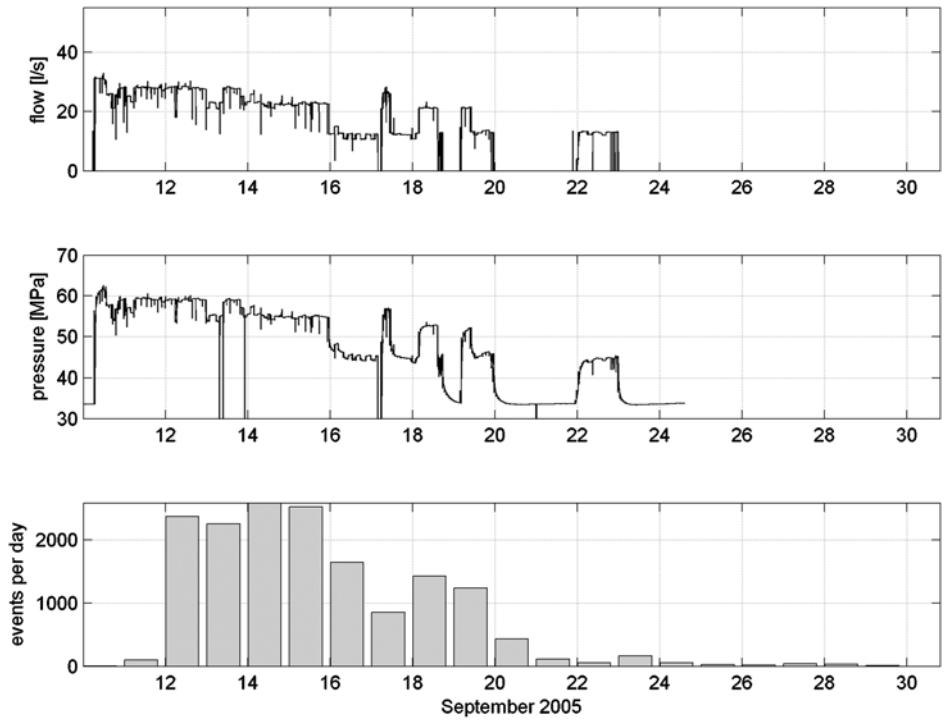

Figure 2. Injection rate (top panel), wellhead pressure (middle panel), and rate of induced events (bottom panel) as a function of time. Approximately 16,000 induced events have been detected in the period shown. Hydraulic injection started on 10 September 2005 at 07:00 UTC. The onset of induced seismicity was delayed by approximately 22 hr.

Fehler and Phillips (1991). Subsequently, displacement spectra were corrected by the average Q-value ($Q = 112 \pm 21$) yielding seismic moments in the range between 10^9 and 10^{13} N m. Magnitudes derived from the seismic moment using the empirical relationship of Bungum *et al.* (1982) are in good agreement with our local magnitude (usually within 0.3 magnitude units), thus confirming our M_L scale.

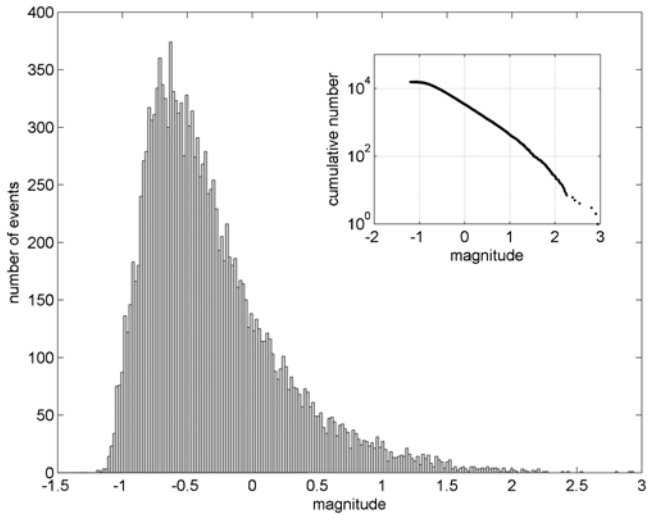

Figure 3. Histogram of event magnitudes (M_L) determined for the 2005 data catalog. The inset shows cumulative number of events as a function of magnitude indicating a b-value of 0.83 in the magnitude range −0.8–1.5.

Moment magnitudes (Hanks and Kanamori, 1979) are similar to M_L for the strongest events but more than one magnitude larger for the smallest events, which is a common observation for microearthquakes (e.g., Jost *et al.*, 1998; see Deichmann [2006] for a comprehensive discussion of potential causes).

Hypocenter Locations

From a total number of 16,017 events, we have determined absolute hypocenter locations for those 8886 events for which at least five *P*- and three *S*-phase onsets could be identified. The hypocenter location procedure follows our previous approach (Baisch, Weidler, Vörös, Wyborn, and DeGraaf, 2006), where absolute hypocenter locations and station residuals are determined iteratively based on a linearized inversion known as Geiger's method (Geiger, 1910). We used the same station dependent seismic velocity model previously calibrated with the 2003 data set by associating early seismicity to the flow exit. Except for the *S*-phase residual at station MW02 (40 msec), all station residuals are on the order of 20 msec or less, indicating that the underlying velocity model is consistent with the current data set.

Figure 4 shows the resulting hypocenter distribution. Average location errors on a 2σ-confidence level are 73, 80, and 113 m into the eastern, northern, and vertical direction, respectively. We note that lateral location errors are slightly larger than those obtained for the 2003 data set, al-

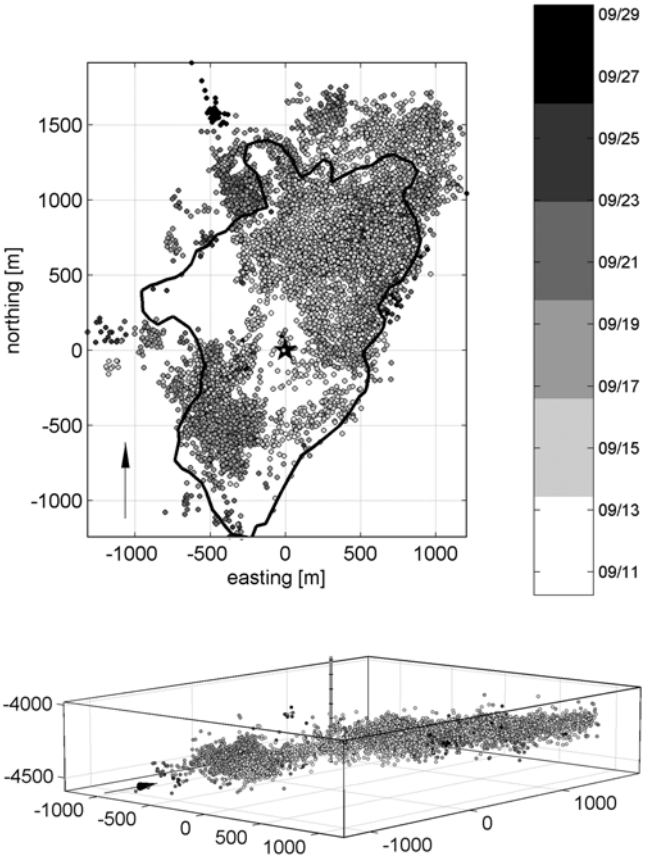

Figure 4. Absolute hypocenter locations in map view (top panel) and in perspective view (bottom panel) looking from the southeast along a best-fit subhorizontal plane. The region of 2003 seismic activity is indicated by a contour line. Gray shading denotes origin time. Coordinates are given with respect to the top of Habanero 1 (indicated by a star in the top panel and a vertical line in the bottom panel).

though additional stations were used. This might reflect the decreasing accuracy of the seismic velocity model with increasing distance to the injection well where the velocity model has been calibrated (Baisch, Weidler, Vörös, Wyborn, and DeGraaf, 2006). On average, the current seismic activity is farther away from the injection well than in 2003, which could explain the observed increase of lateral location errors.

The shape of the hypocenter distribution resembles the zone of seismic activity observed during the previous stimulation. Hypocenters align along a single, subhorizontal flat structure with an apparent vertical extension of 100–150 m. Toward the east and the south, the seismic activity closely follows the boundaries observed previously, whereas a significant growth of the seismically active zone can be observed into the northern and western directions.

Interestingly, very few events are located near the injection well. This is quite different to previous observations where seismicity started at the injection well and then systematically migrated away with increasing time. Here, the seismic activity starts at several positions near the outer boundary of the previously activated zone and, subsequently, migrates toward the injection well, as well as into the opposite direction. This becomes most evident in Figure 5, which shows the spatiotemporal evolution of the first 1854 events. Besides some scattered hypocenters in the central region, seismicity appears highly organized in space and time. Activity starts at several locations near the eastern and northern boundary (open circles). At the northern boundary, the seismic activity predominantly migrates into the direction of the injection well.

Compound Fault-Plane Solution

The spatial hypocenter distribution indicates that the induced seismicity aligns along a single, subhorizontal fracture zone of limited thickness. For the 2003 data, relative hypocenter locations determined for event clusters (see Baisch, Weidler, Vörös, Wyborn, and DeGraaf, 2006) further suggest that the vertical extension of the zone of seismic activity might be at (or below) the meter scale. In this context the induced seismicity occurred on individual patches of a larger scale fracture zone. This hypothesis postulates similar source mechanisms for the individual events.

Because of the extreme sparseness of the seismic monitoring network, single event fault-plane solutions are only loosely constrained. Therefore, our analysis focuses on a compound fault-plane solution. We have determined *P*-wave polarities for all waveforms exhibiting a sufficient signal-to-noise ratio. The resulting polarity patterns are highly systematic. For example, at the two stations to the west, the *P*-wave polarity is negative for nearly all events (Fig. 6). Po-

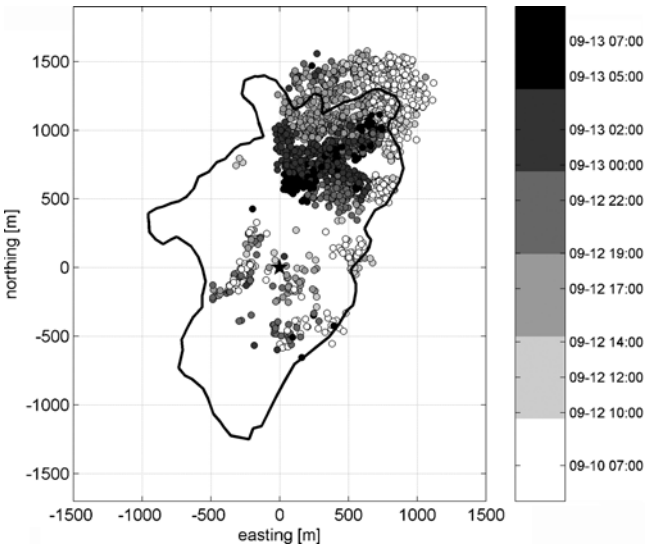

Figure 5. Spatiotemporal distribution of early seismicity in map view. Gray shading denotes origin time. Note that the gray map is saturated at the lower end, displaying all events occurring between 9 September 2003, 07:00 UTC, and 12 September 2003, 10:00 UTC, with white circles. The region of 2003 seismic activity is indicated by a contour line. Note that pronounced seismicity starts at the north eastern rim of the region of previous seismic activity and then migrates back toward the injection well (black star).

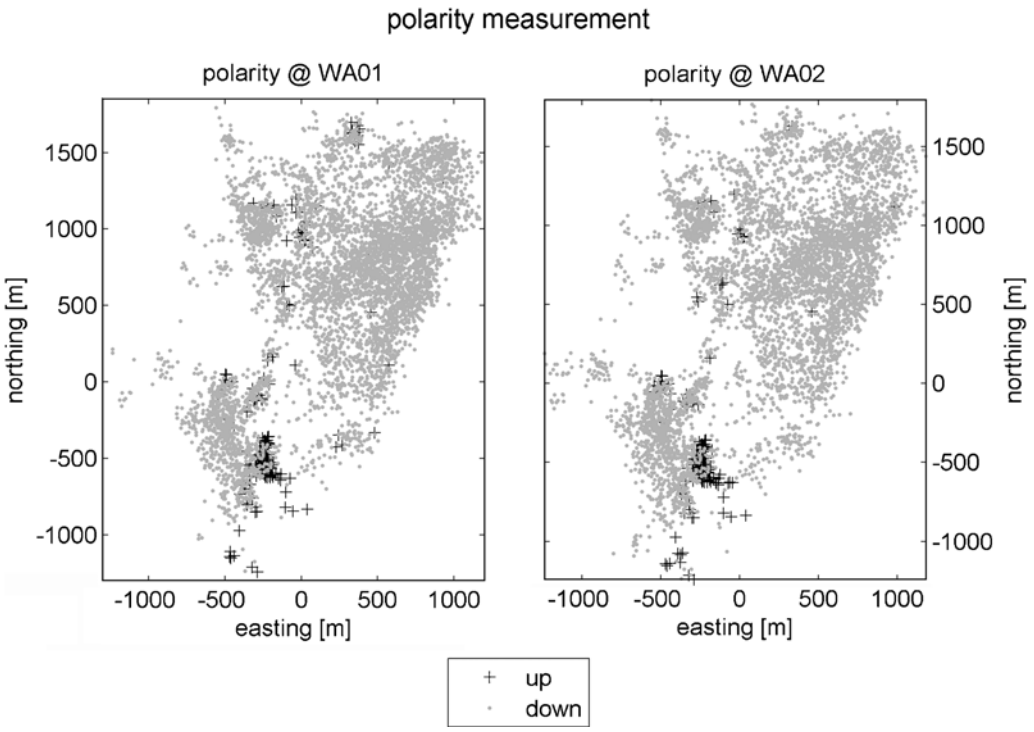

Figure 6. Spatial distribution of hypocenters in map view. The *P*-wave polarity at stations WA01 (left-hand panel) and WA02 (right-hand panel) is indicated according to the legend. Nearly all events exhibit negative polarities at both stations, whereas positive polarities are consistently observed for the same subset of events. The patterns of positive polarities are not strictly identical for both stations because polarities could not always be determined. We note, however, that none of the events exhibiting a positive polarity at one station exhibits a negative polarity at the other station.

larities at the other stations exhibit a similar systematic pattern indicating that most of the events indeed may share a similar fault mechanism. Interestingly, a small group of 208 events consistently exhibits opposite polarities at the outer stations (compare Fig. 6). These events are treated separately in our analysis, and we have subdivided the data set into type I (dominating polarity) and type II (opposite polarity) events.

Considering the extreme case of a set of events with strictly identical fault mechanism, we note that waveform polarities would only depend on the relative coordinates between the stations and the hypocenters. Based on this translation invariance, polarity data from different stations can be combined. Figure 7 shows the distribution of combined polarity data when converted into relative coordinates between hypocenters and station locations. The resulting patterns for type I and type II events are highly consistent, indicating that the whole data set can be characterized by only two different fault mechanisms. We experimented with synthetic polarity data to estimate an upper bound for potential variations of individual fracture orientations that would still lead to the systematic pattern observed in Figure 7. Although this analysis is somewhat subjective, we feel confident that variations of individual fracture orientations cannot be larger than 10°.

A compound fault-plane solution for the type I and type II events has been determined by matching the polarity patterns of Figure 7 with a theoretical *P*-wave radiation pattern (e.g., equation 4.89 in Aki and Richards [2002]). By this we assume a pure double-couple source without isotropic components. This assumption follows our previous interpretation of hydromechanical processes being dominated by shearing rather than mode I opening (Baisch, Weidler, Vörös, Wyborn, and DeGraaf, 2006) and is also consistent with findings from another fluid-injection experiment where isotropic components of the moment tensor were insignificant (Jost *et al.*, 1998).

We performed a grid search over all possible combinations of fault parameters (strike, dip, and rake). At each grid point we computed the theoretical *P*-wave radiation pattern at all (relative) locations defined by the data points in Figure 7. An objective function based on the number of consistent observations weighted by the theoretical *P*-wave amplitude (to downweight observations near the nodal planes) quantifies how much the theoretical polarities match the observed data. To overcome the general ambiguity between fault and auxiliary plane, the best solution is defined as the plane consistent with a thrust faulting regime (the alternative plane would require normal faulting, which is inconsistent with the regional stress field). The best-fitting fault-plane solutions for type I (strike 157°, dip 9°, and rake 65°) and for type II (strike 74°, dip 20°, and rake 150°) events are shown in Figure 7. Note that the compound fault-plane solution of

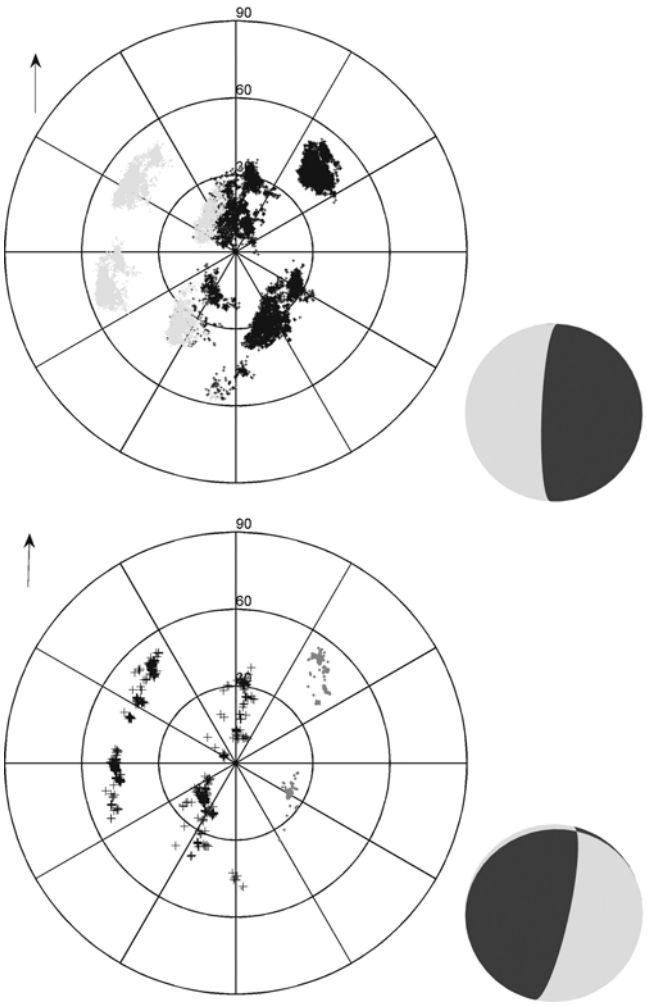

Figure 7. Stereographic projection (upper hemisphere) of the polarity data of type I (top panel) and type II (bottom panel) events. Relative coordinates between stations and hypocenters are used with each hypocenter being located at the coordinate origin. Because of technical problems, only a few polarities could be determined at station WA03. Data from station MCL1, where the instrument polarity is unknown (and might even have changed due to maintenance work), have not been considered. Best-fitting fault-plane solutions are indicated to the right.

type I events is in perfect agreement with the fracture orientation determined previously from the spatial distribution of hypocenters (Baisch, Weidler, Vörös, Wyborn, and DeGraaf, 2006).

Discussion

Hypocenter Locations

We have investigated seismic data of a reservoir restimulation undertaken in 2005 in the Cooper Basin and have presented absolute hypocenter locations and (compound) fault-plane solutions of the induced seismicity. The distribution of the hypocenters closely follows the subhorizontal layer structure identified previously (Baisch, Weidler, Vörös, Wyborn, and DeGraaf, 2006). The location accuracy is on the order of the apparent thickness of the structure, indicating a limited true height. Another production well drilled approximately 550 m northeast of Habanero 1 intersected the layer structure within 22 m of the predicted depth. Televiewer data obtained from the new well shows a heavily fractured zone with a vertical extension of approximately 7 m and further confirms the single layer reservoir model.

Crustal Memory (Kaiser Effect)

The spatial distribution of induced seismicity during restimulation differs significantly from previous observations where seismicity started at the injection well and subsequently migrated away with increasing time (fig. 7 of Baisch, Weidler, Vörös, Wyborn, and DeGraaf, 2006). Here, we notice that only few events are located in the vicinity of the injection well, which is surrounded by a zone of seismic quiescence extending over several hundred meters (Fig. 4, top panel). We interpret this as an expression of the Kaiser effect (Kaiser, 1950), where seismic activity occurs only at those locations where previously experienced fluid pressure values are exceeded. Similar phenomena that could be attributed to the Kaiser effect have been reported from other fluid-injection experiments: Seismic activity induced during restimulation of the 9.1 km deep KTB well (Kontinentale Tiefbohrung, Germany) has been found to be exclusively located at the outer rim of the zone of previous seismic activity indicating stress relaxation in the vicinity of the injection well (Baisch *et al.*, 2002). For the deep geothermal reservoir at Soultz-sous-Forêts (France), as well as for the geothermal reservoir at Bad Urach (Germany), Baisch *et al.* (2004) and Baisch, Weidler, Vörös, and Jung (2006) find a systematic migration of the induced seismicity away from the injection well with increasing time. A similar spatiotemporal evolution of the seismic activity has been observed during hydraulic fracturing in the Cotton Valley gas field (Texas), at the Fenton Hill geothermal site (New Mexico), and in the shallow geothermal reservoir at Soultz-sous-Forêts, which has been interpreted in terms of a back-front of the hydraulic (peak) pressure (Parotidis *et al.*, 2004) equivalent to the Kaiser effect.

The critical fluid pressure P_{crit} required for shearing can be expressed as

$$P_{\text{crit}}(r) = \sigma_n(r) - \frac{\tau(r) - \sum_i^m \delta\tau_i}{\mu(r)}, \qquad (2)$$

where σ_n and τ denote normal and shear stress, respectively, resolved on a fracture patch located at r, and μ is the coefficient of friction. Following the discussion of Baisch and Harjes (2003), stress drop $\delta\tau$ is assumed to be much smaller than τ, and the same fracture patch may shear repeatedly (m times) in the course of increasing fluid pressure. Furthermore, coseismic changes of σ_n are assumed to be of secondary order. At first glance this seems to contradict the idea of stimulation, which aims to increase fracture aperture by shear

displacement, thus increasing σ_n. Laboratory experiments conducted in granite, however, indicate that changes of fracture aperture are an order of magnitude smaller than the applied shear displacement (Chen *et al.*, 2000). Consequently, variations of the normal stresses can be regarded as a secondary order effect.

Maximum fluid pressures measured at the wellhead of Habanero 1 during restimulation are smaller than peak pressures applied in 2003, indicating that the near-well region experienced the highest *in situ* fluid pressure already during the stimulation in 2003. This could explain why only a few events were induced near the injection well during restimulation. Further away from the injection well P_{crit} cannot be measured, and its spatial distribution after the 2003 stimulation is unknown. In particular, dynamic changes of the hydraulic conductivity during the stimulation may result in a complex pattern of P_{crit}. Simple hydraulic considerations, however, require P_{crit} to decrease inside the stimulated zone with increasing distance along any flow path away from the injection well (assuming a constant stress-drop model for all induced events). Bearing this in mind, the Kaiser effect as formulated in equation (2) also provides an explanation for the observed spatiotemporal evolution of the induced seismicity. This is illustrated in Figure 8, which schematically shows the pressure conditions during restimulation. Pressure curves have been derived from an analytical solution for a confined aquifer (Theis, 1935). Based on observed hydraulic parameters, enhanced reservoir permeability and a higher flow rate have been assumed for the reinjection. Because of a shallower spatial gradient during reinjection, pressure conditions remain subcritical everywhere in the reservoir before P_{crit} is reached at the outer rim of the previously stimulated zone (Fig. 8, dotted line). In the course of further pressure increase, seismic activity migrates in both directions, toward and away from the injection well (Fig. 8, line with + symbols). This is consistent with our observations where the onset of induced seismicity is delayed (Fig. 2), its initial location is close to the outer rim of the previous zone of seismic activity, and subsequent migration of the seismic activity exhibits an inward and an outward component (Fig. 5). Clearly, the scenario sketched in Figure 8 is a simplification of a complex process acting during stimulation. It is a static model that does not account for spatial or temporal variations of the hydraulic permeability. However, the underlying principles of (1) decreasing P_{crit} with distance to the

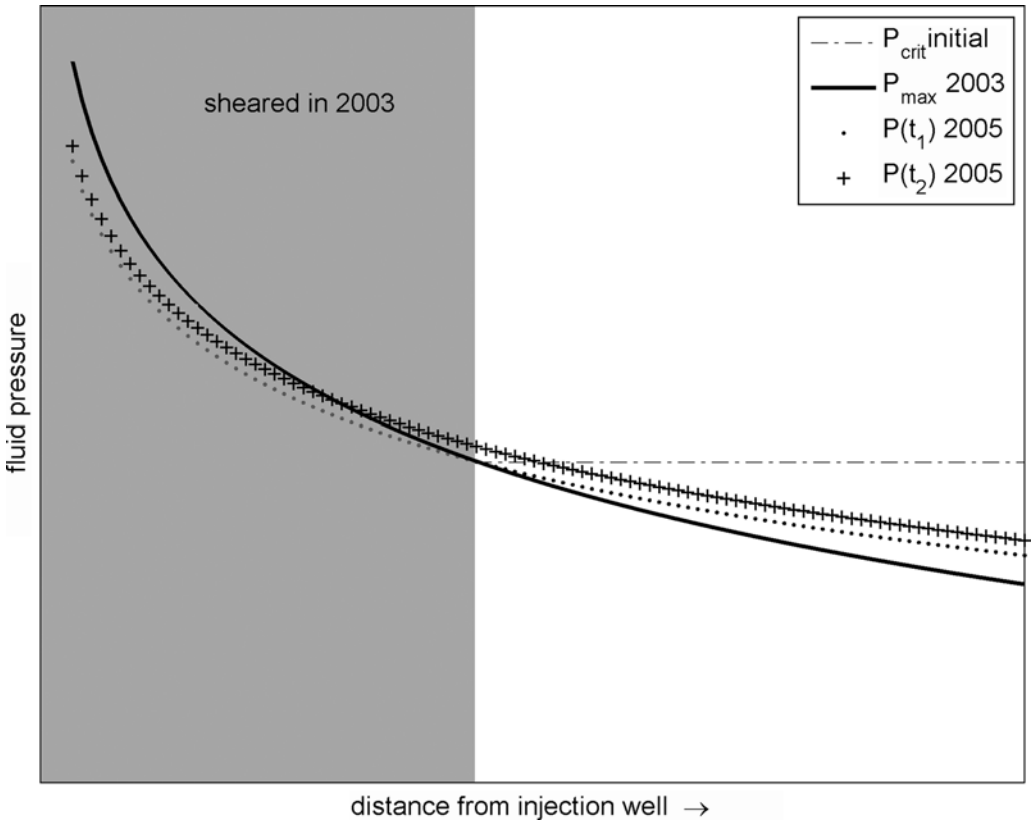

Figure 8. Schematic diagram illustrating critical pressure required for induced seismicity as a function of the distance to the injection well. Dash-dotted line denotes critical pressure for undisturbed rock (i.e., before the stimulation). Black line indicates maximum fluid pressure during the 2003 stimulation, which also defines the critical threshold required for seismic reactivation according to the Kaiser effect. Dotted line denotes pressure distribution at the time when seismicity starts during restimulation. Note that the shallower gradient of the pressure distribution during restimulation results from an increased permeability. Seismicity starts at the outer rim of the zone of previous activity (gray shaded area) and migrates in both directions in the course of further pressure increase (line with + symbols).

injection well and (2) shallower fluid pressure gradients during restimulation are valid also in a more complex model.

Phillips *et al.* (2002) report similar phenomena where seismicity induced during stimulation of hydrocarbon reservoirs systematically migrates in the direction of the injection well. As an explanation, these authors discuss two different models where slip-induced alterations of the local stress field on a very small scale (from meters to tens of meters; S. Phillips, personal comm., 2008) lead to a reverse migration of the seismicity. We note, however, that a similar stress redistribution model is not applicable to the induced seismicity in the Cooper Basin because of the much larger length scales involved.

Fault Mechanisms

The analysis of *P*-wave polarity data indicates extremely similar fault mechanisms for the entire data set, which is consistent with only two different fracture orientations. Compound fault-plane solutions for the two associated event types indicate that both event types are driven by the regional stress field with maximum stress oriented west-northwest–east-southeast (Reynolds *et al.*, 2005). Fault planes of both event types are dipping at a relatively low angle, which is typically observed for large-scale thrust faults. The intersection angle of 21° between the type I and type II fault planes might indicate that the planes have formed as conjugated fractures with the dominating type I events representing a connected, large-scale feature being locally intersected by type II fractures. Given the low shearing angle of the main fracture orientation, type II events could also indicate regions where slight undulations of the main fracture produce slip in the opposite direction.

In light of these interpretations, the fracture complexity in those regions where type II events occur might be larger than assumed previously. To investigate this further, we compared the hypocentral depth of type I and type II events but did not find systematic differences that would indicate vertically separated fracture zones. This is further confirmed by relative hypocenter locations exemplarily determined for neighboring type I and type II events, which provide no evidence for the existence of several distinct fracture zones above the resolution level of 20–30 m (which is the typical location accuracy we obtained for the event combinations tested). Therefore, we conclude that type II events most likely occurred in the immediate vicinity of the main fracture zone, locally defining a more complicated mechanical process zone either in terms of different fracture sets or simply by undulations of the main fracture orientation.

Similar findings are presented by Evans *et al.* (2005) for a geothermal reservoir located at Soultz-sous-Forêts. These authors find evidence for a larger scale fracture zone of 10–20 m width containing a major flow path in the geothermal reservoir. Induced microseismicity occurs within the cataclastic zone on subparallel fractures with relatively low angle to the main structure. Analogous to our interpretation for the Habanero reservoir, Evans *et al.* (2005) conclude that the structure is of natural origin.

Cumulative Shear Slip

In a number of previous studies, the spatial distribution of hypocenters is directly associated with fracture systems and their hydraulic characteristics (e.g., Phillips *et al.*, 1997; Shapiro *et al.*, 1997; Moriya *et al.*, 2002). Several approaches have been suggested to analyze systematic structures within hypocenter distributions (e.g., Fehler *et al.*, 1987; Jones and Stewart, 1997; Nicholson *et al.*, 2000), which are commonly interpreted as hydraulically relevant features. By this, all hypocenters are treated as equivalent points neglecting their individual physical properties. In the context of reservoir stimulation, the induced shear slip is of primary importance. Laboratory experiments indicate a direct relationship between shear slip and fracture permeability enhancement for small shear slip in granite (Chen *et al.*, 2000). Although this relationship may not hold for large shear slip and might even reverse when fracture surface damage occurs (Chen *et al.*, 2000), shear slip still may provide a good proxy for estimating hydraulic conductivity enhancement.

Starzec *et al.* (2000) apply a variogram analysis to investigate the spatial interdependence of slip induced during a stimulation of the upper geothermal reservoir at Soultz-sous-Forêts. They find a correlation between the shape of variograms and the complexity of fracture orientations observed in the near-wellbore region. For the same data set, Bourouis and Bernard (2007) apply a clustering technique to discriminate fault patches that experienced repeated slip. Cumulative seismic slip induced on these patches is found to be on the order of up to 20 cm. In an arbitrary complex fracture network though, it is technically challenging to estimate the total shear slip resulting from multiple seismic events. This is quite different for the present data set where all seismicity occurs on a single layer structure and predominantly exhibits the same slip direction. In this case, the cumulative shear slip associated with multiple events can be estimated by simply adding the individual slip contribution of events with overlapping source area.

To quantify the cumulative slip induced by stimulation activities in the Habanero 1 well, we used empirical relations to estimate source parameters for all events recorded between 6 November 2003 and 13 November 2005. This analysis is critically dependent on the completeness of the seismic catalog. Limitations of the initial recording system caused large data gaps and only 11,068 events out of a total number of 28,011 events were included in our previous catalog for the 2003 stimulation (Baisch, Weidler, Vörös, Wyborn, and DeGraaf, 2006). We have reprocessed this data catalog and included previously disregarded data by applying a constrained hypocenter location procedure where hypocenters are forced to occur on the layer structure. Lateral hypocentral coordinates were calculated for those events for which at

least five *P*-phase onsets could be determined. The average (lateral) location accuracy (1σ-confidence level) is approximately 120 m.

We note that event magnitudes for the 2003 data set have not been determined previously because of the limited dynamic range of the previous monitoring system (Baisch, Weidler, Vörös, Wyborn, and DeGraaf, 2006). To overcome this problem, we have determined the seismic moment for events that were not saturated on the local network recordings and have used the formula of Bungum *et al.* (1982) to estimate magnitudes from the seismic moment. For the strongest 12 events that were recorded by the permanent network of the Australian Government, we used the magnitude assigned by Geosciences Australia (magnitudes between 2.5 and 3.7). Furthermore, we estimated event magnitudes for those 243 events that were not recorded by the permanent network and whose seismograms were at least partially saturated on recordings of the local network. Saturation of the local recording system starts at approximately M_L 1, and the detection threshold of the permanent network is assumed to be M 2.5. We have divided the magnitude range between M 1 and 2.5 into quarter magnitude bins and visually assigned magnitudes based on the seismogram length and the degree of saturation. The accuracy of these event magnitudes probably is not better than 0.5 magnitude units. We estimate that the resulting data catalog of located events is complete down to M_L −0.5, except for the time period between 23 December 2003 and 19 September 2004 for which no data recordings exist.

We determined seismic moment from event magnitudes using the empirical relationship of Bungum *et al.* (1982), which yields, compared to the moment magnitude relation of Hanks and Kanamori (1979), a conservative estimate of the seismic moment (compare with our previous discussion). Subsequently, we applied the circular crack model of Brune (1970) to estimate the source area and slip from the seismic moment. We assumed a constant stress drop of 0.47 MPa, which is the mean stress drop obtained for approximately 6000 events of the 2005 data catalog by fitting source spectra with a ω^2 model. Figure 9 shows the resulting distribution of the cumulative slip. The injection well is surrounded by a high slip region where cumulative slip locally exceeds 9 cm. Slip contributions of individual events are in the range of 0.03–21 mm, indicating that most regions of the reservoir slipped repeatedly for a considerable number of times. The high slip region in the central part of the reservoir exhibits some topography, but cumulative slip values larger than, say, 3 cm are consistently observed along a connected structure with a lateral extension of about 2500 m.

We note that our estimates of the source size and associated slip are strongly dependent on the source model. This is not the case for the product of these two parameters, which is directly proportional to the seismic moment (e.g., Aki and Richards, 2002)

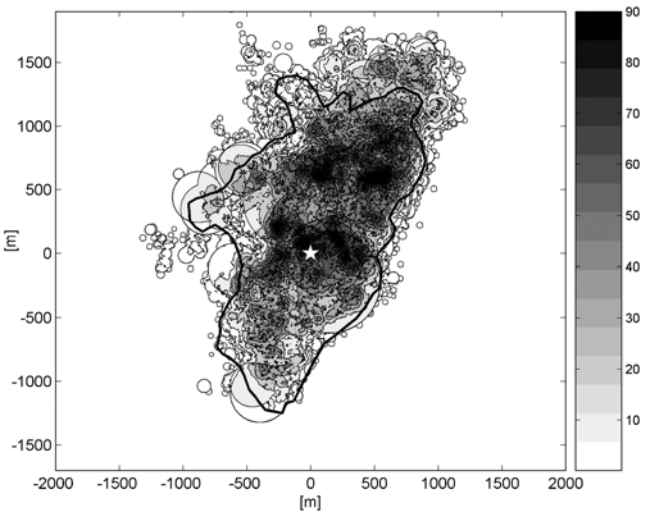

Figure 9. Cumulative shear slip induced between 6 November 2003 and 13 November 2005 in map view. No data exist for the period between 23 December 2003 and 19 September 2004. Shear slip is displayed in millimeters according to the gray map. The star denotes the location of the injection well Habanero 1. The region of 2003 seismic activity is indicated by a contour line. See text for details.

$$M_0 = GAd, \tag{3}$$

with shear modules G, source area A, and average slip d. It is immediately clear that underestimating the source area for a given earthquake with M_0 leads to an overestimate of the amount of slip and vice versa. In our case of multiple, neighboring earthquakes with overlapping source area, uncertainty in one of these parameters tends to average out in the cumulative slip display of Figure 9.

The critical assumption in our estimate of the source parameters is the stress drop. We experimented with different constant stress-drop models in the range of 0.05–1 MPa and found that the general characteristics of the cumulative slip map are not critically depending on the assumed stress drop. The higher the stress drop, the more topography is observed in the cumulative slip distribution and isolated peak values of up to 12 cm can be observed. However, the connected structure with slip values larger than 3 cm remains nearly the same in all our test models.

Another source of error stems from uncertainties associated with the event magnitudes in the 2003 data catalog. Although magnitudes of the largest events (recorded by the permanent national network) are reasonably constrained, event magnitudes in the range of M 1–2.5 might be systematically biased. Downscaling the associated events by 0.5 magnitude units, however, changes the fine structure of the cumulative slip map but not the overall characteristics as discussed previously. Further, it should be noted that the slip distribution of Figure 9 does not distinguish between type I and type II events. Because of the limitations of the initial network, event types could not be determined for most of the data. Assuming that the ratio between type I and type II

observed in the 2005 data is representative also for the 2003 data, then the slip map of Figure 9 includes approximately 3% of type II events. In the 2005 data set we note that the 300 largest magnitude events are type I events and the contribution of type II events on the slip map is of secondary order. Considering the slip contribution of undetected, small magnitude events and the large data gap in the 2003 poststimulation period, we feel that the cumulative slip (Fig. 9) might still be a conservative estimate tending to underestimate the total slip that actually occurred in the reservoir.

High slip on the order of several centimeters has also been reported by Cornet *et al.* (1997) for induced deformation in a geothermal reservoir at Soultz-sous-Forêts. Based on televiewer data, these authors find evidence for slip events larger than 4 cm. Because their maximum magnitudes did not exceed M 1.9, these authors conclude that the slip must have occurred aseismically. For the same reservoir, Evans *et al.* (2005) find evidence for several larger scale fracture zones of tectonic origin constituting the primary permeable paths for fluid migration. These fracture zones showed measurable shear dislocation of millimeters to centimeters (Evans *et al.*, 2005) indicating that shear slip of neighboring (seismic and aseismic) events might have accumulated in a similar way as proposed here for the Habanero reservoir.

Conclusions

We presented a data set of approximately 16,000 microearthquakes induced during the restimulation of a geothermal reservoir in the Cooper Basin, Australia. Seismicity occurred on the same subhorizontal layer structure activated during the initial stimulation and further extended the structure in the course of the stimulation.

No seismicity occurred in the vicinity of the injection well, indicating a crustal memory (Kaiser effect) of the maximum fluid pressure experienced during the first stimulation. An intriguing feature is the observed onset of seismic activity at the outer rim of the previously stimulated zone with subsequent migration toward the injection well. We demonstrated that this behavior can also be attributed to the Kaiser effect when assuming shallower spatial gradients of the fluid overpressure due to permeability enhancement.

Fault mechanisms of the induced seismicity are extremely similar and consistent with the regional stress field acting on a larger scale fracture zone with an orientation as outlined by the hypocenter distribution. This supports an interpretation where seismic activity occurs on patches of the same large-scale fracture zone. In light of this interpretation we determined the cumulative slip by mapping the slip contribution of all events recorded between November 2003 and November 2005 onto the fracture zone. Cumulative shear displacements on the order of several centimeters indicate repeated slip for most fracture patches in the reservoir. Our current observations support previous interpretations of reservoir-induced seismicity being primarily controlled by the fluid overpressures rather than by Coulomb stress transfer.

Data and Resources

Seismograms used in this study were collected using a local network operated by Geodynamics Limited and cannot be released to the public. Seismograms of the largest magnitude events were collected by Geosciences Australia. Data can be obtained at http://www.ga.gov.au/ (last accessed October 2008).

Acknowledgments

We would like to thank Geodynamics Limited for allowing us to publish this study. We gratefully acknowledge comments by Cezar Trifu, Scott Phillips, and an anonymous reviewer who helped to improve the initial manuscript.

References

Aki, K., and P. G. Richards (2002). *Quantitative Seismology*, Second Ed., Univ. Science Books, Sausalito, California.

Baisch, S., and H.-P. Harjes (2003). A model for fluid injection induced seismicity at the KTB, *Geophys. J. Int.* **152,** 160–170.

Baisch, S., M. Bohnhoff, L. Ceranna, Y. Tu, and H.-P. Harjes (2002). Probing the crust to 9 km depth: fluid injection experiments and induced seismicity at the KTB superdeep drilling hole, Germany, *Bull. Seismol. Soc. Am.* **92,** 2369–2380.

Baisch, S., R. Weidler, R. Vörös, H. Tenzer, and D. Teza (2004). Improving hydraulic stimulation efficiency by means of real-time monitoring, in *Proc. of the 29th Workshop on Geothermal Reservoir Engineering*, Stanford, California.

Baisch, S., R. Weidler, R. Vörös, and R. Jung (2006). A conceptual model for post-injection seismicity at Soultz-sous-Forêts, *Geotherm. Resour. Counc. Trans.*, **30,** 601–606.

Baisch, S., R. Weidler, R. Vörös, D. Wyborn, and L. DeGraaf (2006). Induced seismicity during the stimulation of a geothermal HFR reservoir in the Cooper Basin (Australia), *Bull. Seismol. Soc. Am.* **96,** 2242–2256.

Bourouis, S., and P. Bernard (2007). Evidence for coupled seismic and aseismic fault slip during water injection in the geothermal site of Soultz (France), and implications for seismogenic transients, *Geophys. J. Int.* **169,** 723–732.

Brune, J. (1970). Tectonic stress and the spectra of seismic shear waves from earthquakes, *J. Geophys. Res.* **75,** 4997–5009.

Bungum, H., S. Vaage, and E. S. Husebye (1982). The Meloy earthquake sequence, northern Norway: source parameters and their scaling relations, *Bull. Seismol. Soc. Am.* **72,** 197–206.

Chen, Z., S. P. Narayan, Z. Yang, and S. S. Rahman (2000). An experimental investigation of hydraulic behaviour of fractures and joints in granitic rock, *Int. J. Rock Mech. Min. Sci.* **37,** 1061–1071.

Cornet, F. H., J. Helm, H. Poitrenaud, and A. Etchecopar (1997). Seismic and aseismic slips induced by large-scale fluid injections, *Pure Appl. Geophys.* **150,** 563–583.

Deichmann, N. (2006). Local magnitude, a moment revisited, *Bull. Seismol. Soc. Am.* **96,** 1267–1277.

Evans, L., H. Moriya, H. Niitsuma, R. H. Jones, W. S. Phillips, A. Genter, J. Sausse, R. Jung, and R. Baria (2005). Microseismicity and permeability enhancement of hydrogeologic structures during massive fluid injections into granite at 3 km depth at the Soultz HDR site, *Geophys. J. Int.* **160,** 388–412.

Fehler, M., and W. S. Phillips (1991). Simultaneous inversion for Q and source parameters of microearthquakes accompanying hydraulic fracturing in granitic rock, *Bull. Seismol. Soc. Am.* **81,** 553–575.

Fehler, M., L. House, and H. Kaieda (1987). Determining planes along which earthquakes occur: method and application to earthquakes accompanying hydraulic fracturing, *J. Geophys. Res.* **92,** no. B9, 9407–9414.

Geiger, L. (1910). Herdbestimmung bei Erdbeben aus Ankunftszeiten, *K. Ges. Wiss. Goett.* **4,** 331–349.

Gutenberg, B., and C. F. Richter (1956). Earthquake magnitude, intensity, energy and acceleration (second paper), *Bull. Seismol. Soc. Am.* **46,** 105–145.

Hanks, T. C., and H. Kanamori (1979). A moment magnitude scale, *J. Geophys. Res.* **84,** 2348–2350.

Jones, R. H., and R. C. Stewart (1997). A method for determining significant structures in a cloud of earthquakes, *J. Geophys. Res.* **102,** no. B4, 8245–8254.

Jost, M. L., T. Büßelberg, Ö. Jost, and H.-P. Harjes (1998). Source parameters of injection-induced microearthquakes at 9 km depth at the KTB deep drilling site, Germany, *Bull. Seismol. Soc. Am.* **88,** 815–832.

Kaiser, J. (1950). Untersuchungen über das Auftreten von Geräuschen beim Zugversuch, *Ph.D. Thesis*, Fak. f. Maschinenwesen, TH München, Germany.

Moriya, H., N. Katsuhisa, H. Niitsuma, and R. Baria (2002). Detailed fracture system of the Soultz-sous-Forêts HDR field evaluated using microseismic multiplet analysis, *Pure Appl. Geophys.* **159,** 517–541.

Nicholson, T., M. Sambridge, and O. Gudmundsson (2000). On entropy and clustering in earthquake hypocentre distributions, *Geophys. J. Int.* **142,** 37–51.

Parotidis, M., S. A. Shapiro, and E. Rothert (2004). Back front of seismicity induced after termination of borehole fluid injection, *Geophys. Res. Lett.* **31,** L02612, doi 10.1029/2003GL018987.

Phillips, W. S., L. S. House, and M. C. Fehler (1997). Detailed joint structure in a geothermal reservoir from studies of induced microearthquake clusters, *J. Geophys. Res.* **102,** no. B6, 11,745–11,763.

Phillips, W. S., J. T. Rutledge, L. S. House, and M. C. Fehler (2002). Induced microearthquake patterns in hydrocarbon and geothermal reservoirs: six case studies, *Pure Appl. Geophys.* **159,** 345–369.

Reynolds, S. D., S. D. Mildren, R. R. Hillis, J. J. Meyer, and T. Flottmann (2005). Maximum horizontal stress orientations in the Cooper Basin, Australia: implications for plate-scale tectonics and local stress sources, *Geophys. J. Int.* **160,** 331–343.

Shapiro, S., E. Huenges, and G. Borm (1997). Estimating the crust permeability from fluid-injection-induced seismic emission at the KTB site, *Geophys. J. Int.* **131,** F15–F18.

Starzec, P., M. Fehler, R. Baria, and H. Niitsuma (2000). Spatial correlation of seismic slip at the HDR-Soultz geothermal site: qualitative approach, *Bull. Seismol. Soc. Am.* **90,** no. 6, 1528–1534.

Theis, C. V. (1935). The relationship between the lowering of the piezometric surface and the rate and duration of discharge of a well using ground-water storage, *Trans. Am. Geophys. Union* **16,** 519–524.

Q-con GmbH
Marktstrasse 39
76887 Bad Bergzabern, Germany
baisch@q-con.de
(S.B., R.V., R.W.)

Geodynamics Limited
Suite 6, Level 1
19 Lang Parade
Milton, Queensland 4064, Australia
(D.W.)

Manuscript received 5 May 2008